ARTICLE IN PRESS

Extreme Mechanics Letters ▮ (▮▮▮▮) ▮▮▮–▮▮▮

Contents lists available at ScienceDirect

Extreme Mechanics Letters

journal homepage: www.elsevier.com/locate/eml

The stiffness and strength of metamaterials based on the inverse opal architecture

Jefferson J. do Rosário [a,*], Jonathan B. Berger [b], Erica T. Lilleodden [a,c], Robert M. McMeeking [b,d], Gerold A. Schneider [a]

[a] Institute of Advanced Ceramics, Hamburg University of Technology, Denickestrasse 15, D-21073 Hamburg, Germany
[b] Materials Department and Mechanical Engineering Department, University of California, Santa Barbara, CA 93106, USA
[c] Institute of Materials Research, Materials Mechanics, Helmholtz-Zentrum Geesthacht, Max-Planck-Strasse 1, D-21502 Geesthacht, Germany
[d] School of Engineering, University of Aberdeen, King's College, Aberdeen AB24 3UE, Scotland

GRAPHICAL ABSTRACT

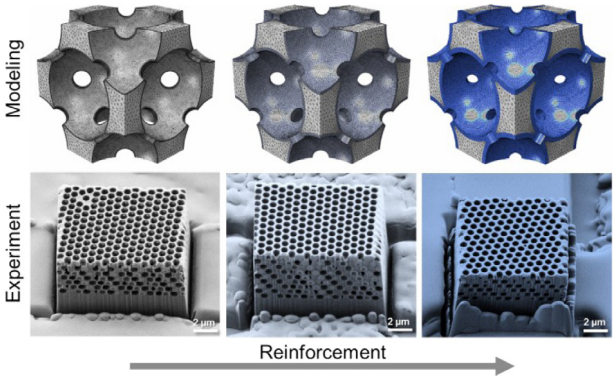

ARTICLE INFO

Article history:
Received 1 March 2016
Received in revised form
31 May 2016
Accepted 19 July 2016
Available online xxxx

Keywords:
Inverse opal
Mechanical metamaterial
Finite element
Self-assembly
Silica
Titania

ABSTRACT

The inverse opal architecture, a class of mechanical metamaterials recently shown to exhibit high specific strength and modulus, is further investigated here using carefully coupled experiments and finite element modeling. We demonstrate that this architecture can be exploited to achieve optimized specific strength and modulus, while simultaneously offering tunable optical bandgaps and large-area fabrication. Starting with a silica inverse opal structure and adding different thicknesses of titania (10–34 nm) the strength was gradually increased from 41 to 410 MPa and the elastic modulus from 1.7 to 8.3 GPa, within densities of 300–1000 kg m^{-3}. Simulations confirmed that the inverse opal structure can outperform the state-of-the-art octet- and isotropic-truss designs in terms of Young's, shear and bulk modulus, as well as in structural efficiency (total stiffness). Simulations also predict stresses in the titania coating and in the silica that are on the order of the theoretical tensile yield stresses at failure, indicating that size effects controlling defect population are responsible for the high strengths.

1. Introduction

The inverse opal (IO) architecture – a design based on the inverse FCC (face-centered cubic) geometry – has recently been

* Corresponding author.
E-mail addresses: jeffersonjean.dorosario@tuhh.de (J.J. do Rosário), g.schneider@tuhh.de (G.A. Schneider).

http://dx.doi.org/10.1016/j.eml.2016.07.006
2352-4316/

presented as a class of mechanical metamaterials that opens a new design space for the development of microscaled lightweight structures [1]. The IO is a known class of photonic crystal, with its characteristic photonic-bandgap controlled by the size of its pores. This combination of classical photonics and high mechanical performance makes this architecture interesting for multi-functional applications.

In the last few years, much effort has been put into developing microscaled lightweight structures with high strength and modulus [2–12]. Novel combinations of design and fabrication techniques have allowed many metamaterials to populate unexplored areas of design space with high specific properties (desired property per density). These metamaterials often rely on a size effect, i.e. the "smaller is stronger" paradigm, to achieve high specific strength at the micrometer and nanometer scale. Many of these experimental investigations of metamaterials are based on the work of Deshpande et al. [13,14] and the octet-truss [3,4,7–10]. Other lattice designs [2,4,6,12] and honeycomb structures [4,12] have also been shown to have interesting properties. Nevertheless, the IO architecture structures have only been outperformed by carbon-based microscaled metamaterials [2,12].

Our previous work showed that the silica based IO structure has substantial stiffness and strength, but the addition of a stiffer and stronger coating (titania) by atomic layer deposition (ALD) is responsible for a significant increase in performance. These materials, uncoated and coated silica IO, possess exceptionally high specific stiffness and strength, and up until recently, are only rivaled by highly anisotropic honeycomb structures [4,12].

In this work, experiments and modeling are used to further understand the properties of IO, and how the addition of a stiff, strong coating affects mechanical properties. Experimentally, we show that the strength and modulus of silica IO can be gradually increased by adding different thicknesses of a titania coating (namely 10, 20 and 34 nm). Average strengths from 41 MPa up to 410 MPa and average elastic moduli from 1.7 GPa up to 8.3 GPa were achieved while varying the density from 330 kg m^{-3} up to 890 kg m^{-3}. Simulations show that the addition of this stiffer, stronger coating can decrease stress concentrations in the silica by 60%. Using simulations, we are able to quantify the structural efficiency and performance of the IO geometry, based on theoretical bounds as metrics. We calculate the Young's, shear and bulk moduli, as well as structural efficiency and isotropy, of the IO geometry. As practical benchmarks for performance, we compare the properties of IO to two high-performance truss geometries, the octet-truss and a truss with maximum stiffness for an isotropic lattice material, recently identified by Gurtner and Durand [15]. The IO is found to have higher structural performance than optimized lattice designs due to its quasi-closed cell geometry which helps to support membrane stresses, while the addition of a robust titania coating increases the absolute performance greatly.

2. Materials and methods

2.1. Opal fabrication

Silica IO films were fabricated by vertical co-assembly based on the procedure described by Hatton et al. [16] 0.6 ml of a 10 w/v% stock suspension of monodispersed colloidal polystyrene (PS) spheres with a diameter of 756 ± 20 nm (Microparticles GmbH) was mixed with 0.450 ml of a hydrolyzed TEOS (tetraethylorthosilicate) solution in deionized water to a total volume of 50 ml. The TEOS solution was composed of 1:1:1.5 ratio by weight of TEOS, 0.10 M HCl and EtOH stirred for 1 h. Soda-lime silica glass substrates were vertically positioned in PTFE beakers containing the prepared suspension. The beakers were placed in a humidity chamber at 60 °C for 3–5 days resulting in a growth rate of 0.5 cm/day of the FCC structure. The substrates were cleaned by soaking in and brushing with an alkaline detergent solution and rinsing with hot tap water and deionized water. Finally, the substrates were dried with filtered nitrogen, and subsequently O_2-plasma cleaned for 20 min. After the co-assembly was carried out the films were calcined at 500 °C for 30 min in order to burn-out the PS template resulting in an inverse opaline structure of amorphous silica. The final IO structure is an inverted FCC elliptical pore arrangement with pore size of 725 nm parallel to the substrate and 670 nm perpendicular to the substrate. The elliptical shape arises from an anisotropic shrinkage upon calcination. The pores are interconnected by holes of approx. 170 nm in diameter. Subsequently, some samples were ALD-coated at 95 °C with an amorphous TiO_2-layer with different thicknesses (10, 20 and 34 nm). The ALD-coating thicknesses were measured in a spectroscopic ellipsometer from a thin film deposited on a silicon wafer during the infiltration with an error of ± 1 nm.

2.2. Opal density determination

The density of the silica IO was estimated by four independent methods: gravimetric, pycnometric and two optical methods. The density of the silica IO coated with TiO_2 was measured by two independent methods: gravimetric and optical. In summary, the densities of pure silica IO and 10, 20 and 34 nm-TiO_2 ALD-coated silica IO are 330, 500, 660 and 890 kg m^{-3}, respectively. The average among different methods lies within a maximum of 10% uncertainty. For more details, see Appendix A (supplementary data).

2.3. Micropillar preparation and microcompression tests

Focused ion beam (FIB) milling was employed to fabricate pillars with square and rectangular cross section using a Nanolab 200 DualBeam microscope (FEI, Co.). Minimal exposure of the fabricated pillars to the Ga ion beam was achieved since no direct imaging of the structure with the ion beam was required. Cross sectional milling was used to fabricate the four planar sides, with the final milling steps imposing beam currents of 300 pA, at an accelerating voltage of 30 kV. A series of microcolumns, all milled into the underlying soda-lime glass substrate, were prepared. This design is advantageous to the analysis of the compression data, since the underlying glass substrate serves as a stiff and hard platen; no filleting at the bottom of the pillar is present, in contrast to pillars that are FIB-milled from the bulk. Here, the deformation is strongly limited to the IO film, with a single deformation volume and in turn a straightforward analysis of the uniaxial stress–strain response.

The compression tests were conducted using a Nanoindenter XP outfitted with a flat ended 60° conical diamond indenter at a constant displacement rate of 10 nm s^{-1} in the (111)-direction to a specified target depth. In all tests a target of 700 nm was chosen, which was in all cases greatly surpassed, as a mechanical instability at the critical failure stress occurred; a large displacement burst up to a few microns typically resulted at failure. In some cases a partial unloading segment prior to failure was included to assess whether an elastic regime is truly present. The stress, σ, and strain, ε, were computed using the load, P, and displacement, h, data along with the geometric parameters, namely the height, H, and the top cross sectional area, A, of the pillars, as measured from SEM micrographs. The stress and strain were computed as $\sigma = P/A$ and $\varepsilon = h/H$, respectively. The elastic modulus was assessed with the continuous stiffness measurement (CSM) method, using a dynamic displacement amplitude of 2 nm at a frequency of 45 Hz superimposed

Please cite this article in press as: J.J. do Rosário, et al., The stiffness and strength of metamaterials based on the inverse opal architecture, Extreme Mechanics Letters (2016), http://dx.doi.org/10.1016/j.eml.2016.07.006

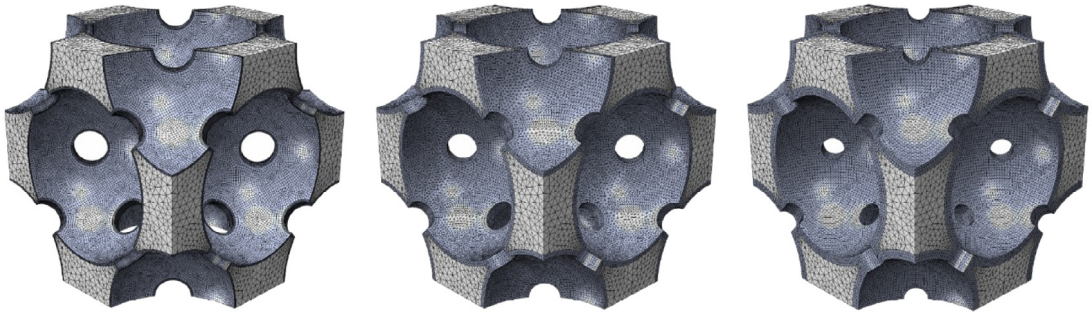

Fig. 1. Unit cells of coated inverse opals, 10, 20 and 35 nm (left to right). The underlying SiO_2 inverse opal geometry remains the same in all calculations. Coatings were composed of 2–4 layers of quadratic elements through the thickness.

during loading. Once full contact between the indenter and sample is achieved, the dynamic stiffness, S_{CSM}, can be used to compute the elastic modulus: $E_{CSM} = S_{CSM}(H/A)$. During the initial loading, the contact area develops leading to an increasing stiffness up until full contact is achieved; the elastic modulus is therefore only established at the plateau. For simplicity, the elastic displacements of the underlying soda-lime glass substrate are ignored since its modulus of is 10 times (or more) greater than that of the inverse opal. These displacements only slightly affect the strain, but do not influence the stress.

Top down images are used to compute the top cross-sectional area. While side-views of the pillars could be used to measure the height of the column, errors associated with the combined tilted view and slight taper of the pillar, along with the difficulty of identifying the top edge of the pillar can lead to significant errors in the measurement of height. Therefore the height was alternatively computed from the known FCC structure of the IO in combination with the SEM images. For an FCC crystal the height, H, in the $\langle 111 \rangle$ direction is given by:

$$H = N_{layers}\left(\frac{\sqrt{3}}{3}\right)\sqrt{2}D \tag{1}$$

where N_{layers} is the number of (111) layers, and D is the diameter of the spherical pore in the $\langle 111 \rangle$, i.e., out-of-plane, direction. For more details, see Appendix A (supplementary data). Pure silica IO and silica IO coated with 10, 20 and 34 nm-TiO_2 pillars have 8.5, 6.5, 8.5 and 5.5 layers of pores along the $\langle 111 \rangle$ direction, respectively. The number of layers yielded heights of 4.7 μm, 3.6 μm, 4.7 μm and 3.0 μm, respectively. Comparing these values to the estimates from the SEM images, we find excellent agreement.

2.4. Modeling

Three types of calculations were performed in order to evaluate performance of the IO structures and create a comparison with the experimental results: (i) plain silica inverse opal, (ii) silica IO coated with 10, 20, 28 and 35 nm of titania and (iii) silica IO coated with 10, 20 and 35 nm of silica, the latter being uncoated systems in essence, allowing for geometric effects to be assessed. As a starting point, the plain silica IO is simulated, and the constitutive inputs were fitted to experiment. Subsequently, the coated IO samples were simulated using the appropriate coating thickness and compared directly to experiments.

2.4.1. Finite element model and boundary conditions

Finite element (FE) models consist of single unit cells subject to periodic boundary conditions. Models are generated using a commercial FE code (ABAQUS CAE, 6.14). Unit cell model geometries for the coated systems are depicted in Fig. 1. FE solutions are computed using the static solver, Abaqus Standard. Nonlinear deformations are allowed using the NLGEOM flag; however, the magnitude of the applied macroscopic strains are small. All models are subject to the same levels of macroscopic strain. We use second order tetrahedral and brick elements, type C3D10 and C3D20 in ABAQUS. Coatings are modeled with 2–4 elements through the coating thickness with negligible influence on the total strain energy. Models are composed of $\sim 7 \times 10^5$ elements. The coating and IO substrate geometry are modeled as separate parts and the TIE command (ABAQUS) used to constrain their relative motion. The boundary nodes on the faces, corners, and edges of the cubic representative volume element (RVE) are required to be periodic. Generating a unit cell octant and using mirroring to form a full unit cell enforces this symmetry.

Periodic sets of boundary nodes experience a relative displacement consistent with the imposed macroscopic strains, enforced through the displacements of "virtual nodes". The complementary reaction forces on the virtual nodes are used to calculate the macroscopic stresses. A full description of this method is given by Danielsson, Parks, and Boyce [17]. To prevent rigid body translations a single node is fixed in place. To prevent rigid body rotations symmetry of the macroscopic strain tensor is enforced. We report the First Piola Kirchhoff stress, which is equivalent to the Cauchy stress when the strains are small.

Model geometries are scaled so that the characteristic length of the cubic RVE, $L = 1.0$. The FCC structure repeats with a characteristic dimension in the $\langle 100 \rangle$ directions of 1025 nm, normalized to 1.0 in the model. The 725 nm pore size in the uncoated SiO_2 system is scaled to 0.707, and the coating thicknesses of 10, 20, 28 and 35 nm, scaled to 0.010, 0.020, 0.027, and 0.034 respectively. The 10, 20, and 35 nm layer thicknesses correspond to the geometries fabricated in this study, and the 28nm layer thickness model is from a previous study [1], where no amorphous coating experimental data are available. The relative density of the SiO_2 structure is, $\bar{\rho}/\rho_S = V_f = 25.5\%$, the layers adding 5.3%, 10.7%, 15.0%, and 18.6%, for a total volume fraction of, $V_f = 30.8\%$, 36.1%, 40.5%, and 44.1%; here the symbol ρ represents the density, V_f is the fraction of the cubic RVE volume that is occupied by the solid phases, and we use the bar notation to denote the effective properties of the metamaterial and the subscript s denotes the properties of the solid. Although the density of the titania layers may vary with the coating thickness, in this analysis we are only concerned with structural efficiency and therefore it is the volume of material in a design, and not its specific properties, that are of interest.

3. Results and discussions

3.1. Experimental characterization of inverse opals

Experimental results are presented in Fig. 2, namely those for plain silica IO and silica IO coated with 10, 20 and 34 nm of amorphous titania. Typical stress vs. strain curves (black lines) and the

Please cite this article in press as: J.J. do Rosário, et al., The stiffness and strength of metamaterials based on the inverse opal architecture, Extreme Mechanics Letters (2016), http://dx.doi.org/10.1016/j.eml.2016.07.006

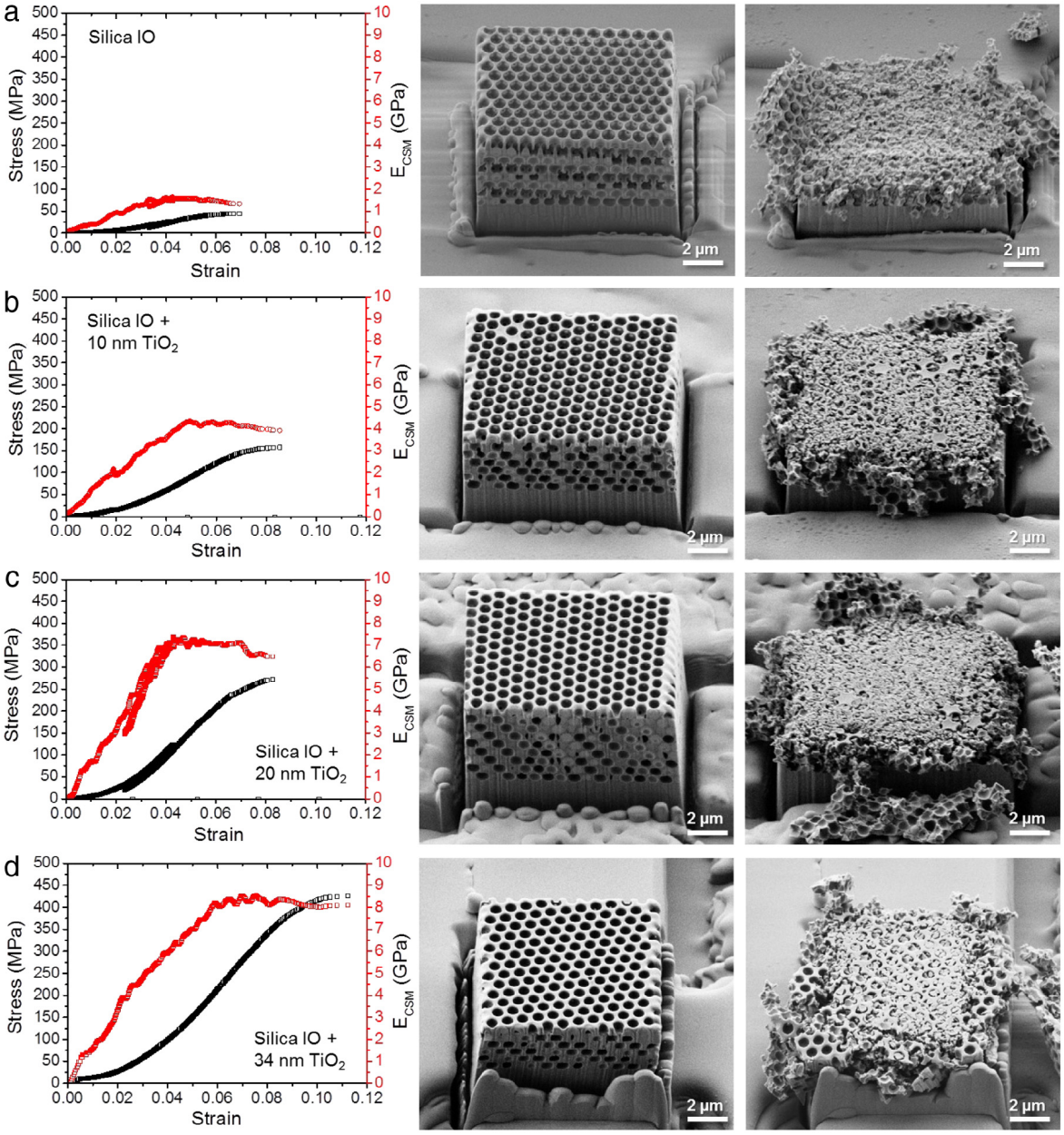

Fig. 2. Typical stress–strain curves and associated elastic modulus (continuous stiffness measurements) and as-fabricated and fractured micropillars for (a) pure silica inverse opal and silica inverse opal coated with (b) 10 nm, (c) 20 nm and (d) 34 nm TiO_2. (For interpretation of the references to color in this figure legend, the reader is referred to the web version of this article.)

associated elastic modulus (continuous stiffness measurements, red lines) show that both strength and elastic modulus increase with reinforcement thickness. In all cases, the target displacement was greatly surpassed. A mechanical instability developed at the critical failure stress and a large displacement jump of a few microns typically resulted. It should be noted, that only the loading and onset of failure portions of the tests are shown. In addition to the mechanical response, Fig. 2 shows typical pillars before and after compression for each type of structure tested. No clear difference in the fracture mechanism can be distinguished from the post-fracture images.

In Fig. 3 the strength and elastic modulus (computed from the loading slope and from CSM) are plotted as a function of the titania thickness. The strength seems to scale linearly with thickness, while the elastic modulus appears to scale linearly up to 20 nm reinforcement, and tends to plateau with only a small increase from 20 to 34 nm of reinforcement. Table 1 presents a summary of results for all samples tested for this work. The strength achieved increased up to 10-fold, going from 41 ± 2 MPa up to 410 ± 31 MPa, in the plain silica IO and the silica coated with 34 nm titania, respectively. This difference corresponds to an increase in specific strength from around 0.125 MPa/(kg m^{-3}) up to 0.451 MPa/(kg m^{-3}). On the other hand, the elastic modulus exhibited a more than 5-fold increase, going from 1.7 ± 0.1 GPa up to 8.3 ± 0.7 GPa, when calculated from stress–strain curve slopes. This difference corresponds to an increase in specific modulus from 5.15 MPa/(kg m^{-3}) up to 9.33 MPa/(kg m^{-3}). The different coatings provide an interesting density range (300–1000 kg m^{-3}) for lightweight materials. Compared with other state-of-the-art strut-based microarchitectures [2–12], only carbon-based designs outperform the titania coated silica IO [2,12].

Please cite this article in press as: J.J. do Rosário, et al., The stiffness and strength of metamaterials based on the inverse opal architecture, Extreme Mechanics Letters (2016), http://dx.doi.org/10.1016/j.eml.2016.07.006

Table 1
Summary of the geometry and the mechanical properties of tested samples.

TiO_2 thickness nm	Porosity	Density kg m^{-3}	Area μm^3	Height μm	Strength MPa	$E_{loading,max}$ GPa	$E_{CSM,\ average}$ GPa
			100.2		40.1	1.7	1.3
0	0.74	330	86.3	4.7	44.4	1.8	1.7
			135.1		40.1	1.7	1.3
Average:					41.3 ± 2.3	1.7 ± 0.1	1.4 ± 0.2
			108.3		156.9	4.1	4.2
10	0.68	500	94.8	3.6	159.7	4.4	4.5
			103.4		144.7	4.0	4.4
Average:					153.8 ± 8.0	4.2 ± 0.2	4.3 ± 0.1
			88.1		246.0	7.0	7.2
20	0.63	660	90.8	4.7	278.3	7.7	6.3
			95.3		289.4	8.0	6.8
Average:					271.2 ± 22.5	7.6 ± 0.5	6.7 ± 0.4
			77.0		424.6	8.6	8.2
			70.9		430.4	8.3	8.5
34	0.56	890	66.9	3.0	441.3	9.0	8.1
			89.7		384.4	8.6	7.2
			79.5		369.2	7.0	7.2
Average:					410.0 ± 31.4	8.3 ± 0.7	7.9 ± 0.6

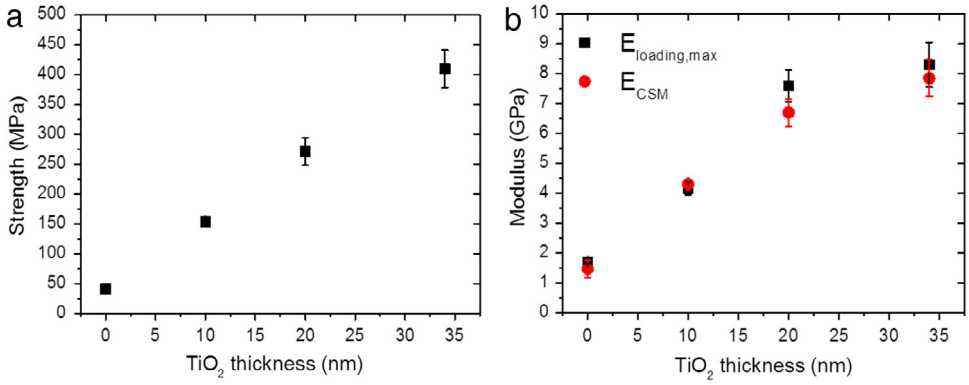

Fig. 3. Summary of the mechanical properties of tested samples: (a) strength and (b) elastic modulus as a function of TiO_2 thickness.

3.2. Modeling

We assume that the silica is isotropic, with its elastic properties thus fully characterized by the Young's modulus E_S, and Poisson's ratio ν_S. IO unit cells, having cubic symmetry, are characterized elastically by three independent elastic constants, Young's modulus $\bar{E}$, shear modulus $\bar{G}$ and Poisson's ratio $\bar{\nu}$, or $\bar{E}$, $\bar{G}$ and bulk modulus $\bar{K}$, all defined relative to a coordinate system with basis vectors aligned with the edges of the cubic RVE shown in Fig. 1. The properties of a-SiO_2 are first assumed to be that of the bulk solid, $E_S = 80$ GPa, $\nu_S = 0.25$, and $\rho_S = 1297$ kg m^{-3}. From these parameters and using the methods described below the properties of the uncoated IO system are calculated to be $\bar{E} = 5.28$ GPa, $\bar{G} = 3.16$ GPa, $\bar{K} = 4.75$ GPa, $\bar{\nu} = 0.32$ and $\bar{\rho} = 593$ kg m^{-3}. The modulus in the $\langle 111 \rangle$ direction is then $\bar{E}_{111} = 7.77$ GPa. In subsequent calculations the solid modulus is scaled to $E_S = 17.52$ GPa, so that the effective $\langle 111 \rangle$ modulus matches the experimentally determined value, $\bar{E}_{111} = E_{CSM} = 1.7$ GPa [1] (Fig. 4).

The modulus of the ALD TiO_2 coatings is known to depend on thickness when thin. We use a linear curve fit to the data of Colombi et al. [18] for coatings with a thickness less than 75 nm. The Young's moduli of the 10, 20, 28 and 35 nm coatings are 48.3, 58.4, 66.5, and 73.6 GPa respectively. The Poisson ratio for all coating thicknesses is taken to be 0.27. Such values are used for the material properties of the titania coatings in the simulations described below.

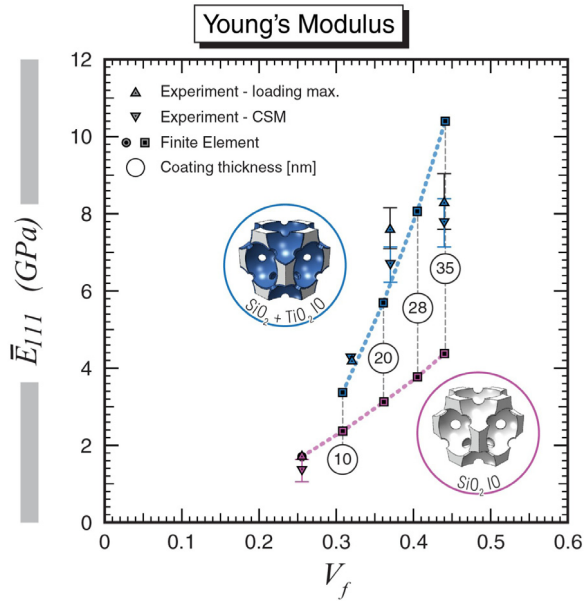

Fig. 4. The modulus in the $\langle 111 \rangle$ direction [experiment (triangles) and FE (squares)] as a function of the solid volume fraction, V_f. The SiO_2 properties are fitted to the uncoated loading slope modulus (circle). (For interpretation of the references to color in this figure legend, the reader is referred to the web version of this article.)

Please cite this article in press as: J.J. do Rosário, et al., The stiffness and strength of metamaterials based on the inverse opal architecture, Extreme Mechanics Letters (2016), http://dx.doi.org/10.1016/j.eml.2016.07.006

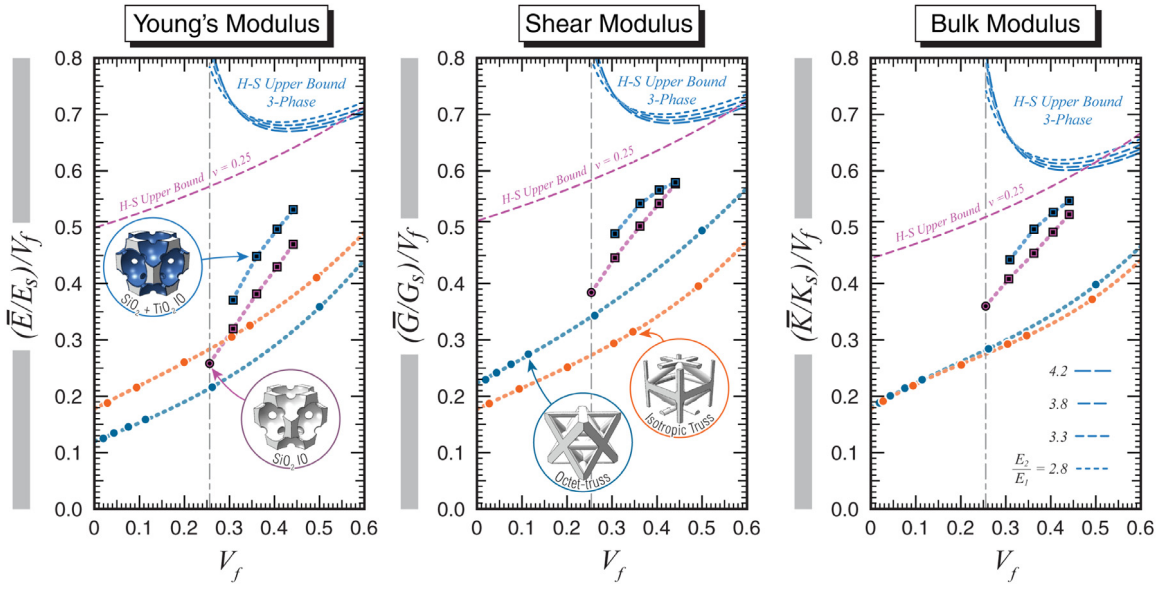

Fig. 5. The computed normalized moduli of inverse opal geometries (solid square) are plotted along with theoretical bounds (purple and blue dashed lines) and the properties of two lattice materials, the octet-truss [14] (solid blue dots) and an isotropic lattice with maximum modulus (solid orange dots) [15]. The coated systems are either silica on silica or titania on silica. Three phase bounds for silica, titania plus voidspace are a function of material properties and the volume fraction of the constituents. There are a set of bounds for the pure SiO2 systems (purple dashed lines), and a group of three-phase bounds for the coated materials (blue dashed lines) whose properties vary with coating thickness. The base, uncoated, system has 25.5% relative density, which becomes the minimum density for the coated systems. (For interpretation of the references to color in this figure legend, the reader is referred to the web version of this article.)

3.2.1. Modulus calculation and elastic characterization

In the simulations the elastic moduli, $\bar{E}$, $\bar{G}$ and $\bar{K}$ are calculated by application of three states of strain, consistent with uniaxial stress, shear stress, and hydrostatic stress. For example, for the case of shear loading, $\bar{\varepsilon}_{12} = \bar{\varepsilon}_{21} = \epsilon$, and all other $\bar{\varepsilon}_{ij}$, $ij = 1, 2, 3$, are unconstrained degrees of freedom; here $\bar{\varepsilon}_{ij}$ are the components of the macroscopic strain tensor, and ϵ is the magnitude of the strain. Alternatively, $\bar{K}$ can be calculated using the Poisson ratio, $\bar{\nu}$, requiring only two calculations to characterize the material. For redundancy, and to plot stress and strain energy distributions, we model hydrostatic loading.

To match FE with experiments, the modulus in the $\langle 111 \rangle$ directions is found using,

$$\frac{1}{E_{111}} = S_{11} - 2\left(S_{11} - S_{12} - \frac{S_{44}}{2}\right)\left(\alpha_1^2\alpha_2^2 + \alpha_2^2\alpha_3^2 + \alpha_3^2\alpha_1^2\right) \qquad (2)$$

where the S_{ij} are components of the elastic compliance matrix and the α_i are the direction cosines between the $\langle 111 \rangle$ direction and the basis vectors of the original coordinate system [19]; for the $\langle 111 \rangle$ direction $\alpha_i = 1/\sqrt{3}$.

Results of the computations are shown in Fig. 4 for coated and uncoated systems, where the coated systems are alternatively those of silica on silica and titania on silica. The case of silica on silica is shown with the results in the lower segment of the figure connected by the pink dashed line, and those for titania on silica in the upper part of the figure by the blue dashed line. It can be seen that the results for the unit cells with titania coatings agree with the experimental data reasonably well, with somewhat better results for the 10 nm and 20 nm thickness than for the 35 nm one.

The best-known theoretical bounds on the modulus of multi-phase composites have been devised by Hashin and Shtrikman [20]. For a two-phase cellular material, composed of a solid and void space, the bounds simplify to [21],

$$\frac{K_{HSU}}{K_s} = \frac{4G_s\,(\bar{\rho}/\rho_s)}{4G_s + 3K_s\,(1 - \bar{\rho}/\rho_s)}, \qquad (3)$$

$$\frac{G_{HSU}}{G_s} = \frac{(9K_s + 8G_s)\,(\bar{\rho}/\rho_s)}{20G_s + 15K_s - 6\,(K_s + 2G_s)\,(\bar{\rho}/\rho_s)}, \qquad (4)$$

where the subscript *HSU* refers to the Hashin–Shtrikman (H–S) upper bound. The bound on Young's modulus,

$$E_{HSU} = \frac{9G_{HSU}K_{HSU}}{3K_{HSU} + G_{HSU}}, \qquad (5)$$

is found from the assumption of linear elasticity with cubic symmetry or isotropic properties. The bounds for a three-phase system, with two solid phases, do not simplify to a similar degree and are instead computed using the algorithm provided by Hashin and Shtrikman [20].

The structural efficiency can be quantified by comparing the effective moduli of the metamaterial to a density equivalent continuum. Plots of $\left(\bar{E}/E_S\right)/\left(\bar{\rho}/\rho_S\right)$, $\left(\bar{G}/G_S\right)/\left(\bar{\rho}/\rho_S\right)$ and $\left(\bar{K}/K_S\right)/\left(\bar{\rho}/\rho_S\right)$ are unity for a material that achieves the Voigt bound, in which stress are uniformly distributed. Fig. 5 compares the efficiency of the uncoated and coated systems to two- and three-phase theoretical upper bounds, and to two high-performance lattice materials. The lattice materials are the octet-truss (OT) [14] and an isotropic truss (IT) with maximum modulus for a lattice material [15]. Systems of SiO_2 coated with SiO_2 are computed to ascertain the role of structural stiffening and strengthening. A description of these results will be given after the introduction of the total stiffness, Eq. (7).

The three-phase theoretical bounds are computed for the four coating thicknesses used in the simulations, beginning at the volume fraction of the uncoated system, $V_f = 25.5\%$. The addition of a small amount of a relatively high modulus phase boosts the theoretical performance most, achieving roughly 80% of the Voigt bound. Past a point of diminishing return, at total volume fractions in the neighborhood of 45%–60%, additional amounts of this phase are relatively detrimental and the two-phase bounds exceed the three-phase bounds. With the addition of $\gtrsim$6% by volume of the second solid phase a lower moduli ratio of the constituents is favored.

The moduli of the amorphous coatings are similar to the anatase (crystalline) coatings [1], and the two material systems occupy the same region of property space. Despite having very high specific stiffness and strength relative to other known materials,

Please cite this article in press as: J.J. do Rosário, et al., The stiffness and strength of metamaterials based on the inverse opal architecture, Extreme Mechanics Letters (2016), http://dx.doi.org/10.1016/j.eml.2016.07.006

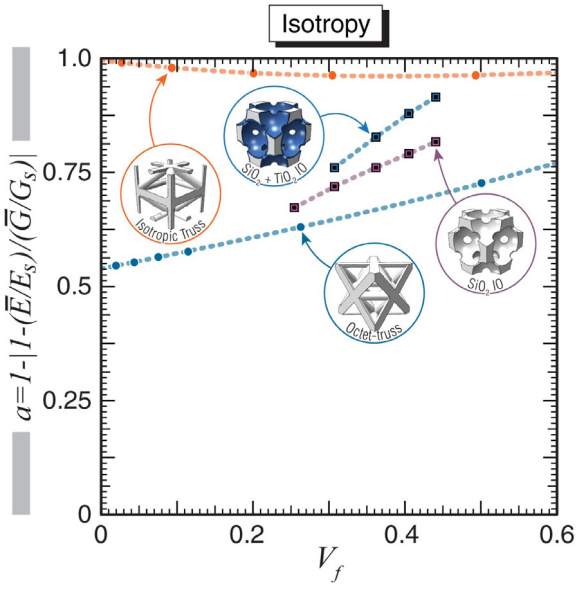

Fig. 6. The anisotropy (Eq. (6)) of the inverse opal material decreases with the addition of the coating. For comparison, the anisotropy of the octet-truss [14] and an isotropic lattice with maximum modulus [15] are plotted.

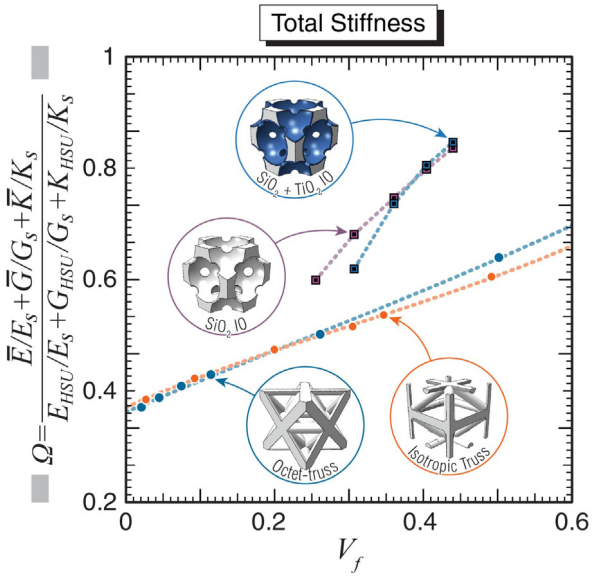

Fig. 7. The inverse opal geometry has greater elastic structural efficiency than optimal lattice materials, the octet-truss [14] and an isotropic lattice with maximum modulus [15]. Addition of a titania coating degrades efficiency relative to theoretical bounds when the coating is thin. As the thickness increases the performance of the two- and three-phase inverse opals converge. Despite significantly different degrees of anisotropy, the performance of the two truss materials is nearly identical.

theoretical bounds indicate the structural performance of the IO is only moderate at low densities, and that significantly higher performing geometries exist. Three-phase systems may have a significant performance advantage over two-phase systems, presenting an opportunity for the development of new materials with novel properties.

3.2.2. Structural anisotropy

To compute the degree of anisotropy we compare the normalized Young's and shear moduli. To preserve the isotropy of a constituent material while adding a void phase, the ratio of the effective moduli must remain constant with relative density. The term,

$$a = 1 - |1 - (E/E_S) / (G/G_S)|\,, \tag{6}$$

is unity for an isotropic metamaterial, and $a \leq 1$, for all metamaterials. The ratio, $(E/E_S) / (G/G_S)$, can be replaced with the Zener anisotropy ratio [19], a measure of anisotropy for cubically symmetric materials, without qualitatively altering results.

The IO geometry is generally anisotropic, being more efficient in shear than axially (Fig. 5). The addition of the coating decreases the anisotropy, independently of the geometric changes (Fig. 6). This is manifest as a relative reduction in shear performance (Fig. 5-middle), where the advantage that the titania coating provides is lost at a total volume fraction, $V_f \approx 44\%$, and the performance of the titania coated and silica on silica systems is the same. Both the titania coated and silica on silica systems are more isotropic than the OT, which was believed, before proper characterization, to be nearly isotropic [22].

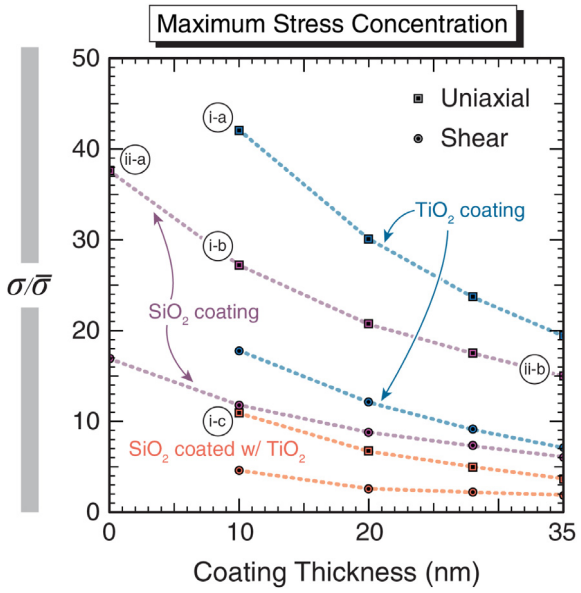

Fig. 8. The addition of a titania coating increases the maximum stress concentration by as much as 55% (i-a, b), but can reduce the maximum stress concentration in the SiO2 by 60% (i-b, c). Changes in geometry alone by addition of a silica coating are responsible for a 45% reduction in stress concentration (ii,a, b).

3.2.3. Structural efficiency

A measure of total structural efficiency can be found by summing the normalized moduli,

$$\Omega = \frac{\bar{E}/E_S + \bar{G}/G_S + \bar{K}/K_S}{E_{HSU}/E_S + G_{HSU}/G_S + K_{HSU}/K_S}, \tag{7}$$

where the subscript s denotes the properties of the constituent or, in the case of a three-phase system, the volume average property of the two solid phases. A material that achieves the H–S upper bound will have $\Omega = 1$. This is effectively a bound on strain energy storage, so that a material that achieves the bound will have a maximum average strain energy density.

The structural efficiency of the IO geometry, as a fraction of theoretical upper bounds, exceeds that of lattice materials (Fig. 7). Despite the significant increase in absolute performance provided by the titania coating, surprisingly, the performance relative to theoretical bounds is seen to only decrease.

The degree of affinity of the deformations, or stretch domination, in a material is the primary factor in determining the

Please cite this article in press as: J.J. do Rosário, et al., The stiffness and strength of metamaterials based on the inverse opal architecture, Extreme Mechanics Letters (2016), http://dx.doi.org/10.1016/j.eml.2016.07.006

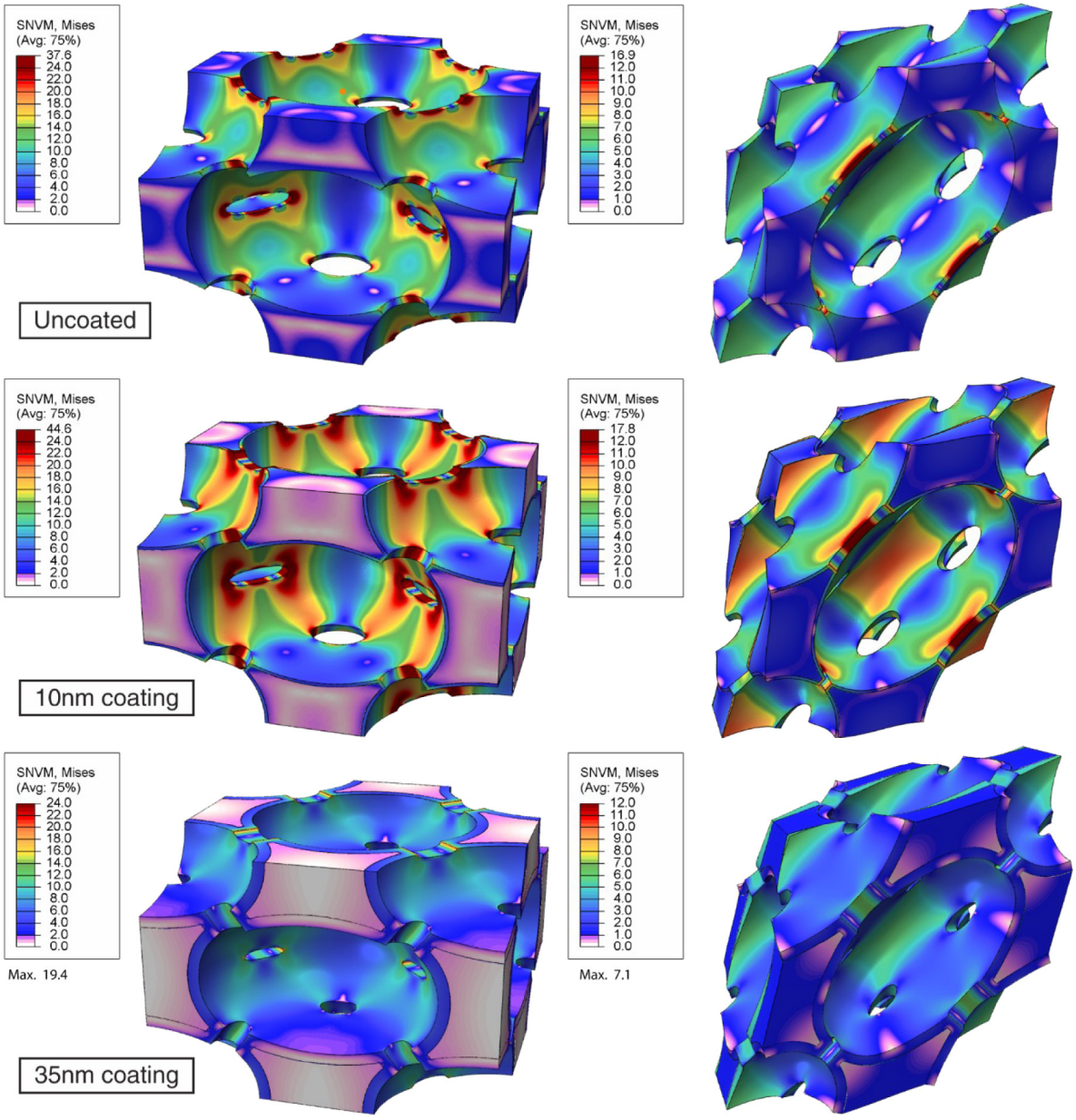

Fig. 9. Stress concentrations, measured in terms of the effective or Mises stress, in the uncoated, 10 and 35 nm coating FE models (top to bottom) under macroscopic uniaxial stress (left) and macroscopic shear stress (right), both defined relative to the coordinate axes aligned with the edges of the cubic representative volume element. All geometries are subject to the same levels of macroscopic strain. The displacements, which are small in reality, are magnified in the images to reveal their nature. The local tensile equivalent stress (TES), i.e. the effective or Mises stress, is normalized by the macroscopic TES. The range of the color contour has been truncated in a compromise that allows a single scale to be used for all three geometries. Stresses are concentrated in thin regions near the intercellular holes that are aligned with the principal stresses. (For interpretation of the references to color in this figure legend, the reader is referred to the web version of this article.)

structural performance [15]. The suboptimal performance of the IO then suggests that significant bending is taking place as it deforms (Fig. 5), and that the highest stresses should primarily be near the surface. A high-performance coating would be expected to increase structural performance as peak stresses will be contained in the more robust material. It is surprising then, that the addition of a higher modulus coating, which increases absolute performance (Fig. 4), and increases the degree of affinity under most of the loading conditions and coating thicknesses (Fig. 5), actually decreases performance relative to theoretical bounds when the coating is thinnest (Fig. 7). The thicker coatings only regain the performance of the silica on silica geometry, never exceeding it by a significant amount.

3.2.4. Maximum stress concentration

Fig. 8 shows the maximum stress concentrations (MSC) as a function of coating thickness for silica IO coated with silica (MSC at outer silica surface) and for silica IO coated with titania. For silica IO coated with titania the MSC in the silica and the titania coating are plotted for each coating thicknesses.

At the experimental fracture strength of the uncoated system, measured in the ⟨111⟩ direction, $\bar{\sigma}_{y,exp} = 41.3$ MPa, FE calculations of uniaxial stress (in the ⟨100⟩ direction) indicate that stress concentrations can be as high as 37.6 (Fig. 8), and local stresses as high as 650 MPa. Stress concentrations are highest near the intercellular holes whose axis is tangential to the loading direction (Fig. 9). There are 12 intercellular holes in each spherical pore, each associated with one of the 12 nearest neighbor pores and

Please cite this article in press as: J.J. do Rosário, et al., The stiffness and strength of metamaterials based on the inverse opal architecture, Extreme Mechanics Letters (2016), http://dx.doi.org/10.1016/j.eml.2016.07.006

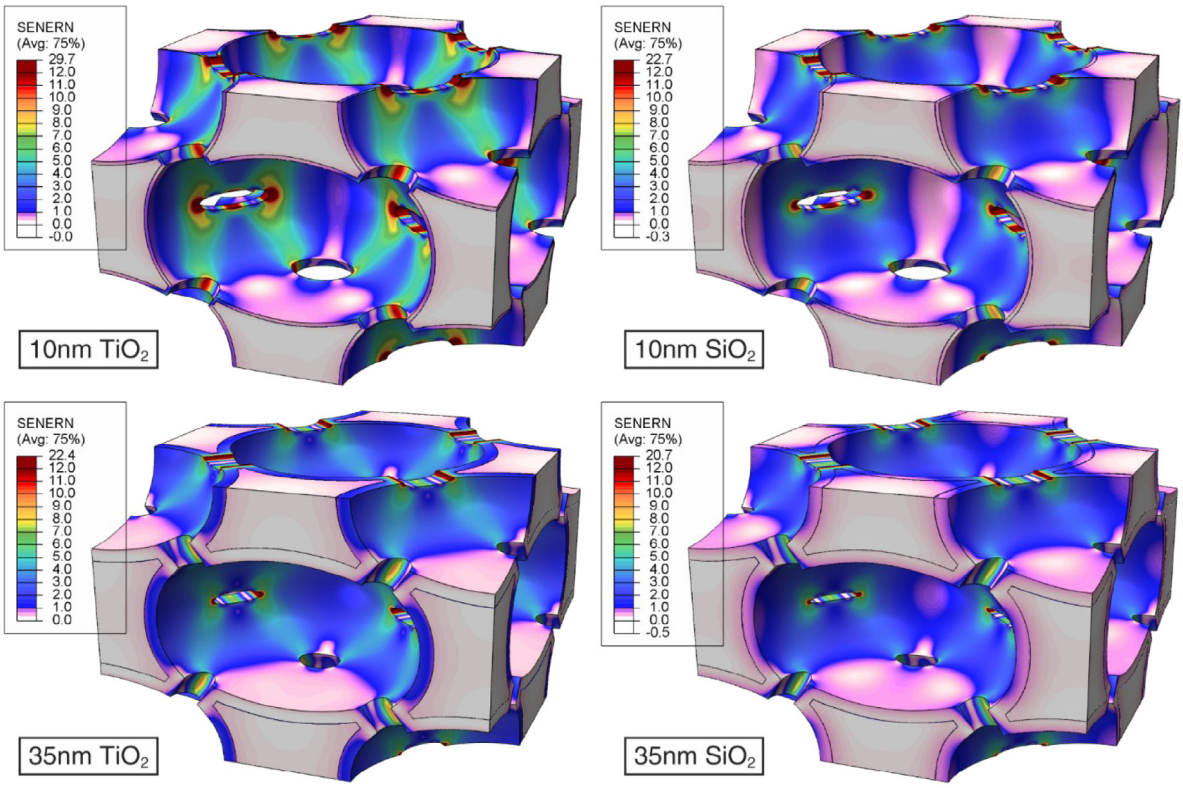

Fig. 10. Strain energy distributions under uniaxial loading relative to coordinate axes aligned with the edges of the cubic representative volume element in the TiO_2 (left) and SiO_2 (right) coated inverse opal systems. Local strain energy density is normalized by the average strain energy density in the solid material. The displacements, which are small in reality, are magnified to reveal their nature. Strains and strain energy are of greatest magnitude in the regions near the intercellular holes. The scale of the color contour is limited to the regime of greatest influence at the sacrifice of fidelity in the extreme regions. (For interpretation of the references to color in this figure legend, the reader is referred to the web version of this article.)

thus connecting nearest neighbor pores together. The periphery of four of the twelve holes are stressed in this manner under uniaxial stress applied in the ⟨111⟩ and ⟨100⟩ directions. Due to the close packed planes of the spherical pores of the ⟨111⟩ type, this critical orientation presents the smallest cross-sectional area for load transmission. Loading in the ⟨111⟩ direction should, therefore, produce the highest stress concentrations and the lowest macroscopic strengths, and be the worst-case scenario in regard to durability of the structure under load.

Despite increasing the absolute strength, the addition of the titania coating increases the maximum stress concentration in the system by 55% with a 10 nm coating, and 30% with a 35 nm coating (Fig. 8). This concentration is, however, limited to the coating, and the maximum stress in the SiO_2 decreases significantly. Changes in geometry alone – the thickening of thin regions and the reduction in the intercellular hole diameter, both by addition of a silica coating – are responsible for a 45% reduction in stress concentration over the range of volume fractions, $V_f = 25\%–44\%$. Similar results were found in our previous study [1].

The stresses in the 10 nm coating are calculated to be in excess of 6.5 GPa under conditions of uniaxial stress in the ⟨111⟩ direction, in excess of 8.2 GPa when the coating is 20 nm thick, and in excess of 7.9 GPa when the coating is 35 nm thick. These stresses are 10% to 15% of E_S and on the order of the theoretical limit [23]. This observation suggests that the material in these regions in the IO that have been produced in practice are defect free. The stresses in the SiO_2 at failure are 1.5 GPa–1.8 GPa and 9%–10% of E_S.

When a macroscopic shear stress is applied relative to the coordinate system with axes aligned with the edges of the RVE the internal stress in the IO is more uniformly distributed, and the magnitude of the maximum concentration, measured in terms of the effective or Mises stress, is significantly lower than under uniaxial stressing (Fig. 9). Similar to uniaxial stressing in the ⟨100⟩ and ⟨111⟩ directions, four of the twelve intercellular holes align with the principal stresses and are the locations of the highest stress concentrations.

3.2.5. Strain energy distributions

Strain energy distributions under uniaxial (Fig. 10) and shear loading (Fig. 11), both defined in terms of coordinate axes aligned with the edges of the RVE, reveal that the thick regions, formed from the interstitial sites in the FCC precursor sphere packings, contribute little to the macroscopic stiffness in both the titania coated and silica on silica systems. Strain energy is primarily stored in the stiff networks of members that align with the principal stresses. Material not stressed in these networks plays only a small role in the storage of elastic strain energy. In the IO geometry these stiff networks are heterogeneous, containing thin and thick regions. The largest concentrations of stress and strain are associated with these thin regions.

4. Conclusions

The results of finite element calculations for the deformation of IO structures agree well with data from experiments. The addition of a titania coating to the silica IO structure produces a measured ten-fold increase in strength, and more than a five-fold increase in modulus in the density range of 300–1000 kg m^{-3}. The strengths and moduli achieved outperform many state-of-the-art strut-based structures whose properties are reported in the literature. Simulations predict that the IO geometry should outperform strut-based structures on the merit of structural efficiency; however, this is not a surprising result. Closed-cell materials are known to outperform open-cell materials, as cell faces constrain the bending

Please cite this article in press as: J.J. do Rosário, et al., The stiffness and strength of metamaterials based on the inverse opal architecture, Extreme Mechanics Letters (2016), http://dx.doi.org/10.1016/j.eml.2016.07.006

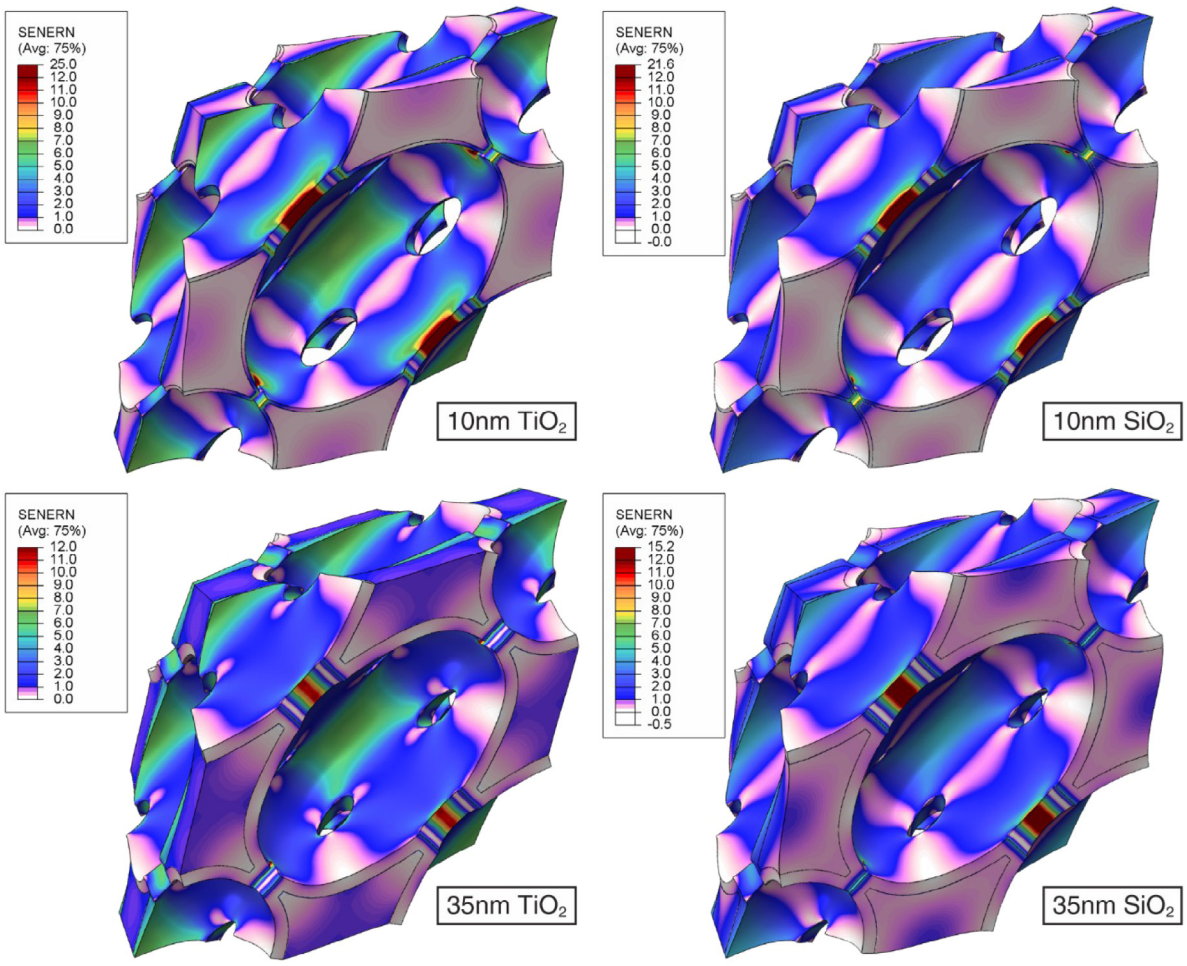

Fig. 11. Strain energy distributions due to shear loading relative to coordinate axes aligned with the edges of the cubic representative volume element in the TiO_2 (left) and SiO_2 (right) coated inverse opal systems. Local strain energy density is normalized by the average strain energy density in the solid material. The scale of the color contour is limited to the regime of greatest influence at the sacrifice of fidelity in the extreme regions. (For interpretation of the references to color in this figure legend, the reader is referred to the web version of this article.)

modes of cell edges. Despite the permeability afforded by the presence of intercellular holes, the IO geometry has some of the features of a closed cell material. The dense interstitial regions are connected by much thinner webs of material, having some of the characteristics of cell edges and faces.

Simulations show that the IO structure can outperform the state-of-the-art octet- and isotropic-truss designs in terms of Young's, shear and bulk modulus, as well as in structural efficiency (total stiffness). Despite these significant properties, theoretical bounds predict that the performance of the coating is suboptimal in the design space of three-phase systems, and that much higher performing geometries may exist. IO are shown to be nearly isotropic, even more so than the extensively studied octet-truss design. Simulations predict stresses in the coating and substrate that are on the order of the theoretical tensile yield stresses at failure, indicating that size effects controlling defect population are responsible for the high strengths.

The high specific modulus and strength of the silica based IO geometry, with its tunable optical bandgaps, and the possibility of fabrication by self-assembly, makes it an attractive system for further development. Optimization of design parameters is possible, as the highest stress concentrations are mitigated substantially by geometric changes, allowing even greater performance to be achieved. Strain energy distributions reveal that the thick regions, associated with the interstitial locations of the precursor spheres, contribute little to the total strain energy storage. Thus one strategy for increasing structural performance may be filling these regions with smaller spheres. Such a strategy has a high likelihood of success as a polydispersed arrangement of hollow spheres is known to achieve the Hashin and Shtrikman [20] upper bound on bulk modulus [21]. Additionally, the introduction of a ductile coating to replace the titania may help dissipate the highest stress concentrations through yielding; a ductile coating may help delay the catastrophic brittle failure seen in experiments. Many opportunities for the development of the IO geometry exist that have yet to be explored. Further developments will allow new systems with novel properties to be developed, and unpopulated regions of design space to be filled.

Acknowledgments

J.J.R., E.T.L. and G.A.S. gratefully acknowledge financial support from the German Research Foundation (DFG) via SFB 986 "M^3", project A6, B4 and C4. We thank Martin Waleczek, Dr. Alexander Yu. Petrov, Dr. Pavel N. Dyachenko and Prof. Manfred Eich for the optical characterization of the density of the inverse opals.

Author contributions

J.J.R. was responsible for the experiments: sample fabrication, testing and analysis. J.B.B. was responsible for the modeling, structural

efficiency characterization and comparison with experimental results. All authors were involved in designing the experiments, analyzing the data, defining the modeling and simulation efforts, assessing the results of the computational simulations and writing the manuscript.

Appendix A. Supplementary data

Supplementary material related to this article can be found online at http://dx.doi.org/10.1016/j.eml.2016.07.006.

References

[1] J.J. do Rosário, E.T. Lilleodden, M. Waleczek, R. Kubrin, A.Yu. Petrov, P.N. Dyachenko, J.E.C. Sabisch, K. Nielsch, N. Huber, M. Eich, G.A. Schneider, Self-Assembled ultra high strength, ultra stiff mechanical metamaterials based on inverse opals, Adv. Eng. Mater. 17 (2015) 1420–1424.
[2] J.-H. Lee, L. Wang, M.C. Boyce, E.L. Thomas, Periodic bicontinuous composites for high specific energy absorption, Nano Lett. 12 (2012) 4392–4396.
[3] D. Jang, L.R. Meza, F. Greer, J.R. Greer, Fabrication and deformation of three-dimensional hollow ceramic nanostructures, Nature Mater. 12 (2013) 893–898.
[4] J. Bauer, S. Hengsbach, I. Tesari, R. Schwaiger, O. Kraft, High-strength cellular ceramic composites with 3D microarchitecture, Proc. Natl. Acad. Sci. USA 111 (2014) 2453–2458.
[5] L.R. Meza, S. Das, J.R. Greer, Strong, lightweight, and recoverable three-dimensional ceramic nanolattices, Science 345 (2014) 1322–1326.
[6] J. Rys, L. Valdevit, T.A. Schaedler, A.J. Jacobsen, W.B. Carter, J.R. Greer, Fabrication and deformation of metallic glass micro-lattices, Adv. Eng. Mater. 16 (2014) 889–896.
[7] X. Zheng, H. Lee, T.H. Weisgraber, M. Shusteff, J. DeOtte, E.B. Duoss, J.D. Kuntz, M.M. Biener, Q. Ge, J.A. Jackson, S.O. Kucheyev, N.X. Fang, C.M. Spadaccini, Ultralight, ultrastiff mechanical metamaterials, Science 344 (2014) 1373–1377.
[8] L.R Meza, A.J Zelhofer, N. Clarke, A.J. Mateos, D.M. Kochmann, J.R. Greer, Resilient 3D hierarchical architected metamaterials, Proc. Natl. Acad. Sci. USA 112 (2015) 11502–11507.
[9] X. Wendy Gu, J.R. Greer, Ultra-strong architected Cu meso-lattices, Extreme Mech. Lett. 2 (2015) 7–14.
[10] J. Bauer, A. Schroer, R. Schwaiger, I. Tesari, C. Lange, L. Valdevit, O. Kraft, Push-to-pull tensile testing of ultra-strong nanoscale ceramic–polymer composites made by additive manufacturing, Extreme Mech. Lett. 3 (2015) 105–112.
[11] L. Montemayor, V. Chernow, J.R. Greer, Materials by design: Using architecture in material design to reach new property spaces, MRS Bull. 40 (2015) 1122–1129.
[12] J. Bauer, A. Schroer, R. Schwaiger, O. Kraft, Approaching theoretical strength in glassy carbon nanolattices, Nature Mater. (2016) http://dx.doi.org/10.1038/nmat4561.
[13] V. Deshpande, M. Ashby, N. Fleck, Foam topology: bending versus stretching dominated architectures, Acta Mater. 49 (2001) 1035–1040.
[14] V. Deshpande, N. Fleck, M. Ashby, Effective properties of the octet-truss lattice material, J. Mech. Phys. Solids 49 (2001) 1747–1769.
[15] G. Gurtner, M. Durand, Stiffest elastic networks, Proc. R. Soc. Lond. Ser. A Math. Phys. Eng. Sci. 470 (2014) 20130611.
[16] B. Hatton, L. Mishchenko, S. Davis, K.H. Sandhage, J. Aizenberg, Assembly of large-area, highly ordered, crack-free inverse opal films, Proc. Natl. Acad. Sci. USA 107 (2010) 10354–10359.
[17] M. Danielsson, D.M. Parks, M.C. Boyce, Three-dimensional micromechanical modeling of voided polymeric materials, J. Mech. Phys. Solids 50 (2002) 351–379.
[18] P. Colombi, P. Bergese, E. Bontempi, L. Borgese, S. Federici, S.S. Keller, Anja Boisen, L.E. Depero, Sensitive determination of the young's modulus of thin films by polymeric microcantilevers, Meas. Sci. Technol. 24 (2013) 125603.
[19] J.F. Nye, Physical Properties of Crystals: Their Representation by Tensors and Matrices, Oxford University Press, 1985.
[20] Z. Hashin, S. Shtrikman, A variational approach to the theory of the elastic behaviour of multiphase materials, J. Mech. Phys. Solids 11 (2) (1963) 127–140.
[21] J.L. Grenestedt, Effective elastic behavior of some models for 'perfect' cellular solids, Int. J. Solids Struct 36 (1999) 1471–1501.
[22] M. Ashby, Hybrid materials to expand the boundaries of material-property space, J. Am. Ceram. Soc. 94 (2011) s3–s14.
[23] N.H. MacMillan, The theoretical strength of solids, J. Mater. Sci. 7 (1972) 239–254.

Please cite this article in press as: J.J. do Rosário, et al., The stiffness and strength of metamaterials based on the inverse opal architecture, Extreme Mechanics Letters (2016), http://dx.doi.org/10.1016/j.eml.2016.07.006